JOURNAL OF GEOPHYSICAL RESEARCH: OCEANS, VOL. 118, 1–18, doi:10.1002/2013JC009261, 2013

Surface circulation in the Gulf of Trieste (northern Adriatic Sea) from radar, model, and ADCP comparisons

Simone Cosoli,[1] Matjaž Ličer,[2] Martin Vodopivec,[2] and Vlado Malačič[2]

Received 9 July 2013; revised 25 October 2013; accepted 28 October 2013.

[1] High resolution high frequency (HF) radar observations of surface currents in the Gulf of Trieste (GoT) are presented and compared to moored subsurface current measurements and to high-resolution simulations from the Northern Adriatic Princeton Ocean Model (NAPOM) oceanographic model. Dominant circulation modes of the GoT were resolved and numerical model capabilities in reconstructing them were assessed. The time frame covers March 2011 through October 2012. NAPOM reconstructs the dominant surface circulation features observed by the radar, such as the general basin-wide cyclonic circulation scheme and the coastal jet outflowing the GoT, but is in general less energetic than radar currents. Comparisons between radar, ADCP, and model currents suggest that the model underestimates originate within the low-frequency, diurnal, semidiurnal, and inertial bands, and that both radar and model currents do not reproduce the diurnal tidal ellipse structure observed by the moored current meter. However, radar-model results for the semidiurnal tides are spatially consistent. Using empirical orthogonal function (EOF) decomposition, the coherent spatial scales and corresponding temporal scales were extracted. Findings suggest that HF radar current observations complement model simulations in regions of enhanced topographic variability where variance of model currents at the surface is distorted by the effects of the sigma layer grid. On the contrary, model results complement radar observations in areas with poor radar coverage, and furthermore provide spatial and temporal continuity of ocean state forecasts.

Citation: Cosoli, S., M. Ličer, M. Vodopivec, and V. Malačič (2013), Surface circulation in the Gulf of Trieste (northern Adriatic Sea) from radar, model, and ADCP comparisons, *J. Geophys. Res. Oceans*, *118*, doi:10.1002/2013JC009261.

1. Introduction

[2] The Gulf of Trieste (GoT) is a small-scale (approximately 25 km × 25 km wide) and shallow (maximum depth ∼38 m) basin located in the northeastern corner of the northern Adriatic Sea (Figure 1) to which it is connected through its western side. In spite of its relatively small size the circulation dynamics in the gulf are of high strategic importance since the GoT hosts two of the largest cargo shipping ports (Koper and Trieste) in the Adriatic. Following *Simpson* [1997], the GoT can be classified as a region of freshwater influence (ROFI) since the circulation in the area responds to a number of complex processes controlled by tides, wind, waves, and variations in river discharge that significantly vary on a year-to-year time scale. A persistent freshwater tongue originating from the Isonzo/Soča river outflow constitutes the major freshwater input in the area and characterizes surface outflow along the Italian coastline in the northern flank [*Malačič et al*., 2006]. Several studies have also shown the presence of a seasonal thermohaline-driven cyclonic gyre generated by the Po river in the Northern Adriatic, which may also impact the freshwater input in the GoT during summer and autumn [*Artegiani et al*., 1997].

[3] Based on a discontinuous series of vertical current profiles collected in the GoT during the 1979–1981 period, *Stravisi* [1983a, 1983b] proposed a layered gyre-type circulation pattern with a weak (2–3 cm/s) permanent cyclonic (counterclockwise) circulation in the bottom layer (below 10 m depth), and an alternating, wind-driven, cyclonic (anticyclonic) flow in the surface (approximately 5 m thick) layer.

[4] Tidal oscillations in the Adriatic Sea originate primarily from remote forcing in the Ionian and Mediterranean seas and enter the Adriatic basin through the Otranto strait [*Defant*, 1914; *Malačič et al*., 2000; *Cushman-Roisin and Naimie*, 2002; *Janeković and Kuzmić*, 2005; *Book et al*., 2009]. The dominant tides manifest themselves at semidiurnal and diurnal frequencies and can be interpreted, respectively, in terms of a double-Kelvin wave traveling in opposite directions and presenting an amphidromic point in the mid-Adriatic (the semidiurnal tides); and a combination

[1]Istituto Nazionale di Oceanografia e di Geofisica Sperimentale—OGS, Sgonico, Trieste, Italy.
[2]National Institute of Biology, Marine Biology Station Piran, Piran, Slovenia

Corresponding author: S. Cosoli, Istituto Nazionale di Oceanografia e Geofisica Sperimentale, Borgo Grotta Gigante 42/c, IT-34010 Sgonico, Trieste, Italy. (scosoli@ogs.trieste.it)

2169-9275/13/10.1002/2013JC009261

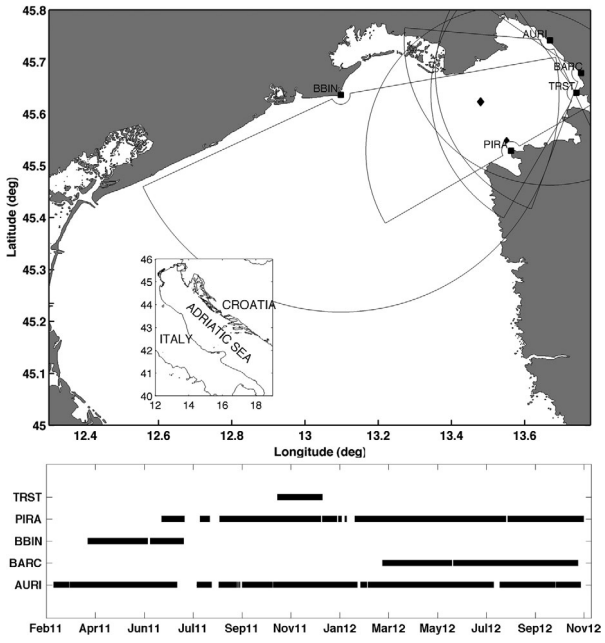

Figure 1. Location of the Gulf of Trieste, northern Adriatic Sea, with locations of the HF radar sites, marked as black squares, and corresponding radial spatial and temporal coverages. Location of the VIDA buoy in front of PIRA radar site is shown (smaller black diamond), along with the location of the grid point in the gulf with the maximum temporal coverage (about 86%—larger black diamond).

of both Kelvin waves and topographic waves propagating across the Adriatic Sea in the diurnal frequency band. The four major semidiurnal (M_2, S_2, N_2, and K_2) and the three major diurnal (K_1, O_1, and P_1) constituents exhibit similar intragroup behavior, patterned after the M_2 and K_1 responses [*Janeković and Kuzmić*, 2005]. At the level of Adriatic Sea, tidal contribution to the overall variability is in general relatively weak, becoming important only in proximity of tidally dominated inlets [*Chavanne et al*., 2007; *Kovačević et al*., 2004; *Cosoli et al*., 2012b], and specifically the GoT area. Similarly, tidal contribution to transport (through residual tides) is deemed negligible [*Cushman-Roisin and Naimie*, 2002; *Malačič and Viezzoli*, 2000].

[5] Despite being potentially intense in terms of discharge rates [*Covelli et al*., 2004], the Isonzo/Soča River presents a discontinuous, impulsive-type regime which—apart from a narrow freshwater belt—limits its influence in the GoT to events localized in time. As a consequence, the basin-wide circulation in the GoT is mainly driven by meteorological forcing, especially by the cold "bora" and, to a minor extent, by the warmer "sirocco" wind during windy seasons (mostly fall and winter), and by thermohaline processes during summer. Bora is a fetch-limited katabatic and gusty wind blowing from NE, occurring more frequently during winter season and in the northern sector of the Adriatic Sea and presents a peculiar topographically controlled jet-type pattern with maxima in the GoT, south of the southern tip of the Istrian peninsula (the Bay of Kvarner) and less intense along the eastern border of the central and southern Adriatic Sea. On the other hand, sirocco blows from the SE sector along the Adriatic Sea main axis with less gustiness than the bora, bringing warm and humid air masses in the area. The bora jet was shown to be responsible for the greatest mean net heat loss of the entire Adriatic Sea [*Dorman et al*., 2006; *Raicich et al*., 2013], as well as for vertical mixing of the water column, renewal of intermediate and bottom water masses and for a significant reduction of residence time in the GoT [*Boldrin et al*., 2009; *Querin et al*., 2006].

[6] Circulation in the Adriatic Sea in general, and in the GoT in particular, has been primarily investigated through a wide set of 2-D and 3-D numerical models, with idealized or more realistic forcing and bathymetry [see for instance, *Malačič et al*., 2012, for a more detailed review]. Experimental campaigns have also been conducted that made use of ADCP current meters, Lagrangian drifters or intensive field CTD casts, and high-frequency (HF) radar observations, but these field experiments were focused primarily on the open-sea and neglected to some extent the GoT area. Amongst them are: ELNA—Eutrophic Limits of the Northern Adriatic [*Hopkins et al*., 1999]; ACE—Adriatic Circulation Experiment [*Book et al*., 2007]; DOLCEVITA (Dynamics of Localized Currents and Eddy Variability in the Adriatic). General findings suggest the presence of a GoT-wide cyclonic (counterclockwise) circulation in the lower part of the water column with entrance along the southern (Slovenian) coast and an intensified outflow along the northern (Italian) coast.

[7] In this study, a long (about 2 years) record of near-surface (approximate measurement depth 0.5 m), high-resolution (1 h temporal resolution; 1.5 km × 1.5 km horizontal resolution) high-frequency radar current measurements is presented, and compared to high-resolution (1 h temporal resolution; ∼0.6 km × 0.6 km horizontal resolution) numerical simulations and pointwise high-resolution (1 h temporal resolution; 1 m vertical resolution) ADCP measurements of subsurface currents in the GoT area.

[8] HF radar data can now be considered a reliable benchmark for numerical circulation models and for validation of tidal current models [e.g., *Chapman and Graber*, 1997; *Kohut and Glenn*, 2003; *Emery et al*., 2004, *Davies et al*., 2000, *Erofeeva et al*., 2003, *Mau et al*., 2007, *Rosenfeld et al*., 2009, *Wang et al*., 2009, *Chavanne et al*., 2007]. In the Adriatic Sea, HF radars were deployed starting from 1997 in the central area offshore Ancona [*Kovaević et al*., 2000], and spread later to various subdomains in the northern half of the Adriatic [*Chavanne et al*., 2007; *Kovačević et al*., 2004; *Gačić et al*., 2009; *Mihanović et al*., 2011; *Cosoli et al*., 2012b].

[9] In this work, HF radar data of surface currents are analyzed to characterize dominant circulation features in the GoT, as well as to verify model capabilities in reproducing them. The work is organized as follows. Section 2 introduces the observational data set, the description and setup of the numerical model, while section 3 contains the data-model comparison metrics. Section 4 contains the data-model comparison, and section 5 presents results and discussions. Finally, main findings are summarized in section 6.

2. Observational Data and Model Description

2.1. HF Radar Data

[10] Surface current data used in this study were collected as part of the "TOSCA—Tracking Oil Spill and

Coastal Awareness" initiative operating within the European Union's INTERREG MED program. The network consisted of SeaSonde HF radars deployed in the Gulf of Trieste (GoT) area, a marginal semienclosed basin in the northeastern most part of the Adriatic Sea (Figure 1).

[11] HF radars measure near-surface currents by analyzing the echo of the transmitted signal after it is reflected from ocean waves with wavelength half the wavelength of the transmitted electromagnetic signal [*Paduan and Graber*, 1997]. At the operating frequency of 25 MHz, the backscatter is due to gravity waves having wavelength of approximately 6 m, and current measurements are representative of a layer of approximately 0.5 m [*Stewart and Joy*, 1974]. Two or more systems are required to resolve the two-dimensional flow field in the area of common signal overlap. Ocean current maps are derived on a regular grid by the least-square fitting radial velocities from at least two stations in the area of common overlap [*Gurgel*, 1994], provided some constraints on the intersecting beam geometry are satisfied in order to reduce errors of geometrical dilution of precision (GDOP) [*Chapman and Graber*, 1997]. For the GoT, hourly surface current fields were derived on a Cartesian grid with a horizontal resolution of 1.5 km by computing the best-fit vector velocity components using all radial data falling within a 3 km distance for each grid point.

[12] The HF radar sites changed locations during the project time window, but ensured an adequate coverage within the GoT (Figure 1). Two systems, located, respectively, at Punta Tagliamento at the mouth of the Tagliamento river (site code: BBIN) outside the bay, and at Aurisina (site code: AURI) at the closed end of the GoT, constituted the observing network over the period March to June 2011, when a third station was added located on top of Piran Rt Madona lighthouse (site code: PIRA). This radar experienced some major failure during February 2012, which compromised radar functioning and gave discontinuous coverage in that month. BBIN station was dismantled at the end of July 2011 and the HF radar was temporarily installed in the Trieste harbor's pilot station (site code: TRST) for the period November 2011 to January 2012. At the end of February 2012, a system was installed on the roof of the "Saturnia Rowing Club" in Barcola, Trieste (site code: BARC). The HF radar network thus ensured an almost continuous coverage in time from March 2011 through November 2012 (Figure 1).

[13] Radars operated in the 25 MHz frequency band with 5° resolution in angle and 1.0 km resolution in range, with the exception of the BBIN station where the range resolution was set to 1.5 km to maximize coverage in the GoT area. The resulting overall offshore range was 30 km for AURI, PIRA, TRST, and BARC stations, and 46 km for BBIN radar.

[14] Radar radial data were quality-controlled by their signal-to-noise ratio (SNR) values as described in *Cosoli et al*. [2012a], and radial velocities exceeding 1 m s^{-1} maximum speed were removed prior to the least-squares fit. Grid points with unfavorable intersecting beam geometry ($\theta \leq 30°$; $\theta \geq 150°$, with θ the angle of the intersecting beams at each grid point) were excluded during the mapping procedure. The resulting velocity time series at each grid point were further quality-checked as described in *Kovačević et al*. [2004].

[15] Spatial gaps in current vector maps, due either to the sparseness of the radial data arising from limitations in the SeaSonde's direction finding algorithm [*Barrick and Lipa*, 1997; *Laws et al*., 2000; *de Paolo and Terrill*, 2007], external interferences, GDOP, site-to-site baseline problems, or the quality check procedures, were filled using a distance-weighted interpolation of data from the nearest neighboring cells. The procedure ensured a temporal data coverage for up to 80% of the observing period in the majority of the GoT.

[16] Validation studies performed in coastal areas surrounding the GoT have investigated the performances of the HF radar systems in the northern Adriatic Sea. Comparisons of vector currents with in situ velocity observations and radar-to-radar baseline studies [*Cosoli et al*., 2005, 2010, 2012b] provided comparison metrics consistent with many locations elsewhere. Correlation and RMS differences between the radar and current meter radial velocity time series are found in the range $r = [0.53; 0.65]$ and [7.5 cm/s; 9.9 cm/s], with bearing errors in the range [10°; 20°]. Significant reduction in radar spatial coverage has been observed during strong northeasterly (bora) wind pulses in their initial stages, as already documented in *Cosoli et al*. [2010].

2.2. Subsurface Mooring Data

[17] A 600 kHz standalone Nortek AS AWAC acoustic profiler, deployed at the seafloor in proximity of the coastal buoy VIDA (13°33′1,89″ E, 45°32′55,68″ N, www.buoy.mbss.org) about 2 km from the PIRA radar station (Figure 1), provided pointwise subsurface currents for the January 2011 to November 2012 period. The current meter was placed at 0.5 m above the bottom, and measured currents for 10 min at intervals of 30 min over 21 depth cells with a 1 m vertical spacing. It was connected to the control unit on board the buoy with a 60 m cable and transmitted data through an Ethernet microwave link every 30 min to the land station where they were inserted into a dedicated database.

[18] To avoid sidelobe contaminations the first cell next to the seafloor and the two top-most cells near the sea-surface were removed [*Malačič et al*., 2012]. Additionally, one more cell close to surface was removed to account for the vertical variability of sea surface level due to tides. Subsurface measurements were thus available for 17 out of 21 cells with a temporal resolution of 30 min at a vertical resolution of 1 m covering the 3–20 m depth range. Quality-controls were performed on the 30 min data as described in *Kovačević et al*. [2004] to remove as many anomalous values as possible. Hourly current values were finally computed from the quality-controlled 30 min data by averaging three sequential half-hour observations in the time range ±30 min around each hour in order to match more closely the radar processing scheme.

2.3. The Northern Adriatic Princeton Ocean Model (NAPOM)

[19] NAPOM is an operational version of Princeton Ocean Model (POM), set up in the Northern Adriatic [*Malačič et al*., 2012], and running daily at the Slovenian Environment Agency (ARSO). Model domain extends between 44.478° N–45.82° N, and 12.20° E and 13.91° E.

Its horizontal grid is orthogonal with an Arakawa C differencing scheme with a horizontal resolution of roughly 600 m, while its vertical grid consists of 11 sigma-layers at relative levels 0.0, −0.06, −0.15, −0.26, −0.37, −0.48, −0.59, −0.70, −0.81, −0.91, −1.0, reaching a maximum depth of roughly 53 m. NAPOM mode splitting is inherited from POM: the external time step, used for the barotropic mode computation, is set to 9 s; the internal time step, used for the baroclinic mode calculations, is set to 90 s. These time steps and grid resolutions were set to satisfy the Courant-Friedrichs-Lewy condition of numerical stability. The model is unidirectionally nested in the Adriatic Sea Forecasting System (AFS), run by INGV Bologna http://gnoo.bo.ingv.it/afs), which provides NAPOM with initial and lateral open boundary conditions. These conditions are interpolated in space and time according to the NAPOM spatial and temporal resolution. Vertical turbulence closure scheme is the usual 2.5 Mellor-Yamada, while horizontal diffusion is treated using the standard Smagorinsky formula.

[20] Atmospheric input for NAPOM consisted of meridional and zonal 10 m winds, mean sea-level pressures, vertical heat, air humidity, and precipitation, provided by the atmospheric forecasting system ALADIN/SI, which ran operationally at 9.5 km horizontal resolution at the ARSO [*Pristov et al*., 2011] during the radar measurement period. ALADIN/SI hourly output fields were downscaled to NAPOM numerical grid and linearly interpolated in time to the ocean model's internal time step of 90 s. The model results presented here used measured discharges and climatological temperatures of the Po River, and climatological discharges and temperatures of all other major rivers flowing into the model domain (Po, Isonzo/Soča, Timavo, Dragonja, Rižana, Mirna). Tides are implemented in NAPOM as modulations of the elevation and vertically averaged velocities at the open boundaries. Flather open boundary condition is applied. The amplitudes and phases of tidal constituents M_2, K_2, N_2, S_2, K_1, P_1, and O_1 are taken into account at each open boundary point. The constituents were calculated from a coarser tidal model of the entire Adriatic and interpolated to the locations of the model open boundary [*Malačič and Viezzoli*, 2000, *Malačič et al*., 2000, 2012]. Further details about the model setup are available elsewhere [e.g., *Malačič et al*., 2012].

[21] NAPOM model currents used in this study were vertically linearly interpolated from sigma-coordinates to a 0.5 m horizontal *z*-layer depth at each model output time step for the entire HF radar observation window (March 2011 to October 2012). NAPOM hourly surface currents were mapped onto the radar grid by choosing the closest model grid point for each location.

3. Data-Model Comparison Metrics

[22] The comparison metrics comprises the calculation of mean biases and RMS differences, variance distribution, scalar and vector correlation, empirical orthogonal function (EOF) decomposition, tidal and spectral analyses.

[23] The magnitude and the angular misfit (R, θ) of the vector correlation between the observed and the modeled currents are estimated at each grid point following *Kundu* [1976]. The following correlation and the mean angular veering between current vectors were applied:

$$R = \frac{\langle u_r u_m + v_r v_m \rangle + i\langle u_r v_m - v_r u_m \rangle}{\langle u_r^2 + v_r^2 \rangle^{1/2} \langle u_m^2 + v_m^2 \rangle^{1/2}} \tag{1}$$

$$\theta = \tan^{-1} \frac{\langle u_r v_m - v_r u_m \rangle}{\langle u_r u_m + v_r v_m \rangle} \tag{2}$$

where u, v are the demeaned zonal and meridional components of the surface vectors for the radar (indexed r) and the model (indexed m) time series, respectively, $i = \sqrt{-1}$, and $<\bullet>$ the ensemble-average operator. In addition, mean biases $<u_r, v_r> - <u_m, v_m>$, scalar correlations and RMS differences between current components are computed.

[24] To determine the extent to which radar data and model reproduce the dominant spatial and temporal scales, time-averaged currents and corresponding variance levels are computed on a monthly basis. The dominant modes of variability and the corresponding time scales are extracted from radar and model data through a combination of empirical orthogonal function (EOF) decomposition and spectral analysis. EOF modes are extracted from the real-valued current time series [*Kaihatu et al*., 1998] using the singular-value decomposition of the covariance matrix for grid points having adequate temporal continuity. The analysis gives a set of real-valued spatial maps (the EOF modes) that represent spatially coherent structures, and the corresponding temporal coefficient documenting their time variability. The real-valued EOF decomposition of hourly radar and model current fields, performed on $M = 262$ grid points for the time frame May 2011 to October 2012, provided $2M = 524$ EOF modes. Apart from removing the temporal averaged currents at each grid point included in the analysis, no filtering was applied to the velocity time series.

[25] In the frequency domain, variance-preserving rotary auto-spectra [*Emery and Thompson*, 2001] are computed for both observations and model simulations, in order to extract the dominant frequency components. Model-to-data discrepancies were additionally explored using power spectral analyses, carried out at each grid point over the resolvable frequency range through the squared coherence spectrum, γ^2:

$$\gamma^2(f) = \frac{P_{rm}^2}{P_{rr} P_{mm}} \tag{3}$$

where P_{rr} and P_{mm} represent the spectral density distributions of the individual time series r (radar), m (model), and P_{rm} is their cross-spectral density distribution. Smooth estimates of the spectral densities are obtained following the modified-periodogram approach using 512 h data segments with a 50% overlap and a Hanning window, yielding the largest resolvable period around 10.7 days.

[26] For both radar and model data, a least-squares tidal analysis was performed on the complex-valued current vectors using the t_tide Matlab package [*Pawlovitz et al*., 2002]. Amplitudes of major and minor axes, ellipses inclinations and phase angles, together with the corresponding 95% confidence levels for the seven major tidal

constituents for the Adriatic Sea area M_2, S_2, K_2, N_2, K_1, O_1, and P_1) were extracted at each grid point. Confidence intervals for ellipse parameters were computed following an uncorrelated colored-noise model. Nontidal currents were derived subtracting the synthetic tidal time series from the original hourly observations. Currents at selected frequency bands (subtidal low-frequency, diurnal, semidiurnal, and inertial) were also extracted using a 4th order Butterworth filter with cutoff frequencies of, respectively, $v < 0.0039$ cph (low-frequency; $T > 256$, $h = 10.7$ days), $v = [0.038, 0.045]$ cph (diurnal; $T \sim 22$–26 h), $v = [0.0714, 0.10]$ cph (semidiurnal; $T \sim 10$–14 h), and $v = [0.055, 0.062]$ cph (inertial; $T \sim 16$–18 h).

[27] To avoid biases from temporally sparse data, analyses are performed on temporally overlapping time series of at least two radar transmitters at each grid point; temporal interpolation is performed for the spectral analyses and the frequency-band filtering. EOF analysis is limited to the time period May 2011 to October 2012 due to poor spatial coverage in the GoT from the BBIN station.

4. Data-Model Comparison Results

4.1. Time-Domain Comparisons

[28] Time-averaged radar and model surface current patterns for the period March 2011 to October 2012 and the corresponding current variance levels, along with the monthly averaged current patterns for November 2011 and April 2012 are presented in Figure 2. A feature common to the two time-averaged current maps is the relatively intense (~7 cm/s radar maximum speed; 12 cm/s model maximum speed) jet-like structure outflowing the GoT area along the Italian coastline in the northern sector, which extends approximately to the midline of the GoT. Model results reproduce this key feature well. To the south, the model suggests a weaker inflow along the southern border of the GoT thus describing a cyclonic (counterclockwise) circulation cell, which however is almost missing in the radar time-averaged currents. According to the sequence of model monthly averaged current maps (not shown due to clarity), the cyclonic turn is a stable and persistent circulation feature in the GoT, which is only occasionally detected in the radar monthly maps. For example, this pattern is present both in radar and model currents in November 2011, but not during April 2012 (Figure 2). On the other hand, the jet-like outflow feature in the northern sector is observed in both radar and model monthly current maps, although in general model fields present stronger currents than the radar data. Radar monthly maps for April (Figure 2) and May (not shown) 2012 show an intense anticyclonic recirculation cell in the interior of the GoT area, presumably driven by an intense variability of the outflow from the Isonzo/Soča River), which creates an inertial bulb of fresh water around the outlet during increased outflow [*Malačič et al*., 1999; *Malacic and Petelin*, 2009]. This water body may detach from a coastline into a freshwater "blob" during weak outflow afterward. This feature is not observed in the corresponding model monthly maps. This probably stems from the fact that Isonzo/Soča (and other) river discharges in the model are set to monthly climatological values, which tend to average out the short-term discharge peaks.

[29] One important difference is between the variance levels of radar and model current fields, and their spatial distribution in the GoT. Though being more intense in their time-averaged values, modeled currents have lower monthly variances, especially in the southern half of the GoT (Figure 2) than radar currents (except for February 2012). The model clusters current variances in a relatively narrow strip in the northern flank of the GoT, while radar variances are more evenly distributed within the Gulf. The model in particular concentrates variances in two major spots, the first located in proximity of the GoT entrance and the second in the GoT interior in front of the Isonzo/Soca river outlet. The latter can be interpreted as the ROFI variability with riverine contribution. The first is most likely an artifact of the model induced by the bathymetry gradient in that area as further illuminated in section 5.

[30] Temporally, radar and model show a similar seasonal pattern in the distribution of monthly spatially averaged variance of currents (Figure 3) with maxima during spring-summer (May-June-July) and lower values in fall and winter season (November-December-January). Both data sets show a significant increase in current variance in February 2012 when a strong (~20 m/s) and prolonged (~2 weeks) bora wind episode occurred, with model variances exceeding corresponding values from radar currents due presumably to the lack of radar measurements.

[31] A decomposition into low-frequency, diurnal, semidiurnal and inertial signals (respectively: $v < 0.0039$ cph, or $T > 256$ h; $v \sim 0.042$ cph, or $T \sim 24$ h; $v \sim 0.083$ cph, or $T \sim 12$ h and $f \sim 0.058$ cph, or $T \sim 17$ h) suggest that there is a solid match between model and radar variances in a low-frequency band and that discrepancies between radar and model variances occur at diurnal, inertial, and semidiurnal frequencies, which are seasonally modulated. Although surface wind driven currents reach lower values in the model, it is interesting to note that the space averaged variance during the extreme wind event in February 2012 is higher in the model when the radar coverage was intermittent. This holds also for model currents in the outflowing coastal jet along the Italian coast. Spatial patterns of the complex correlation coefficient and the veering (or, phase) angle, along with scalar correlation and RMS differences for the radar-model zonal and meridional vector components are presented in Figure 4. The magnitude of the complex correlation coefficient between the observed and modeled currents exceeds 0.5 in front of the Grado lagoon (northwestern boundary of the GoT), with the lowest values along the southern coastline where the radar radial coverage was poor. The distribution of phase angles shows that 80% of the veering angles were between $-18°$ and $+16°$. Analysis reveals that magnitudes of the scalar correlation coefficients for the zonal (u, east-west) and the meridional (v, north-south) component can be as high as 0.53 and 0.40, respectively, and spatial distribution for the zonal component scalar correlation matches that of the complex cross-correlation coefficient (Figure 4). Root-mean-square (RMS) values of velocity component differences (Figure 4) and mean biases (not shown) of the zonal and meridional velocities show similar distributions, with discrepancies between the model and radar

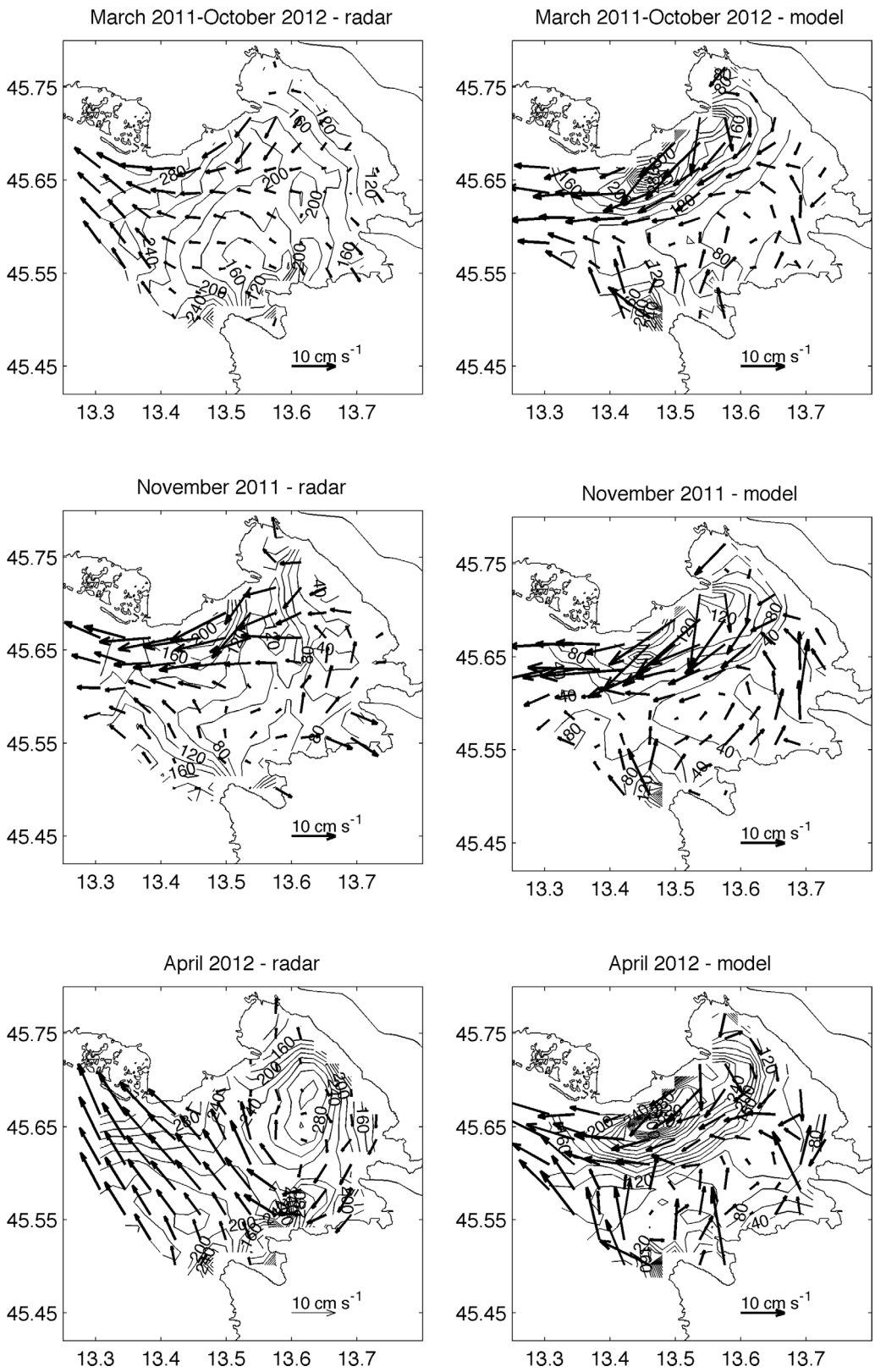

Figure 2. Time-averaged current patterns for the time window (top) March 2011–October 2012 with the corresponding variance levels for (left) radar and (right) model currents. The monthly averaged patterns for radar and model currents for (middle) November 2011 and (bottom) April 2012 are given, respectively. Units are cm s^{-1} for currents, cm^2 s^{-2} for variances. Current vectors were subsampled every two grid points for readability.

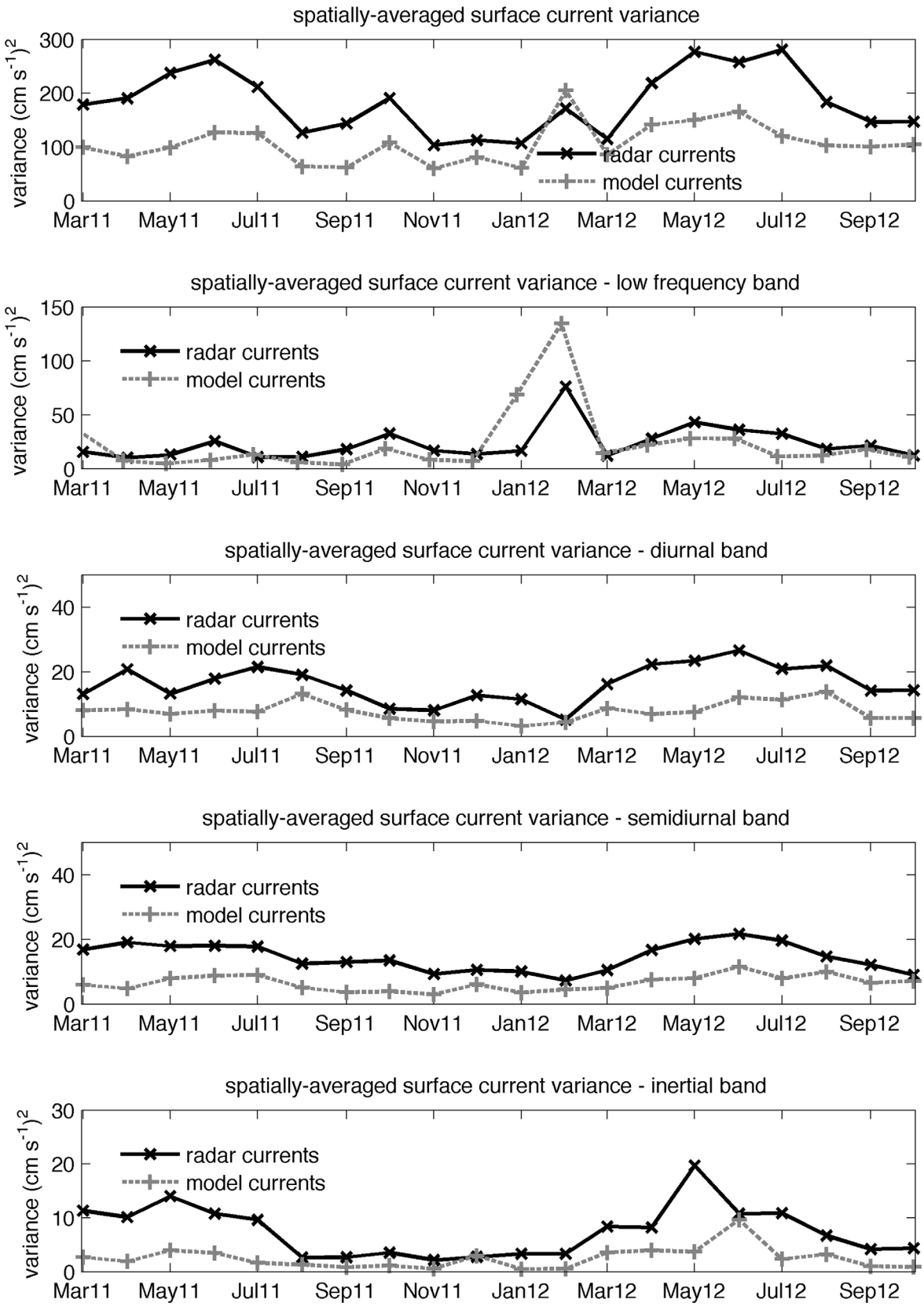

Figure 3. (top to bottom) Time series of spatially averaged monthly variances for radar data (black lines) and model (dotted lines) currents, and corresponding values for the low-passed ($T > 256$ h), diurnal ($T \sim 24$ h), semidiurnal ($T \sim 12$ h), and inertial ($T \sim 17$ h) frequency bands.

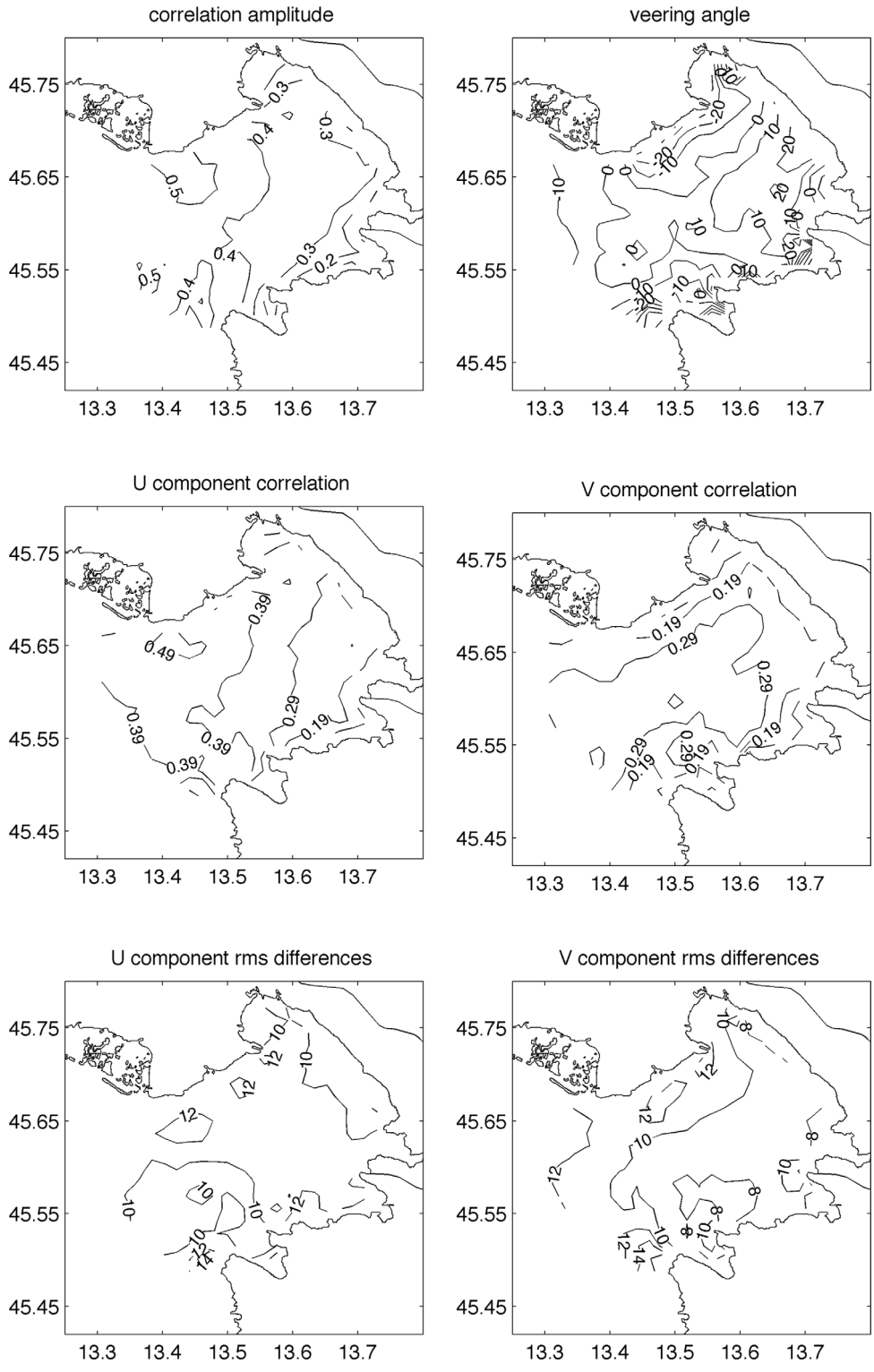

Figure 4. (top to bottom, left to right) The spatial patterns of the complex correlation coefficient and the veering angle (degrees); the distribution of the scalar correlation coefficient between radar and model current components; and the RMS differences contour plots for the radar-model zonal and meridional vector components.

values in the northern (shallower) part of the GoT. In general, 80% of the RMS differences for u are found between 9.8 and 11.1 cm/s, and 80% of the RMS differences for v lie between 8.6 and 11.2 cm/s. Calculated biases are lower, and in the ranges $(-2.6,4.5)$ cm/s and $(-3.7, 3.4)$ cm/s for the two velocity components.

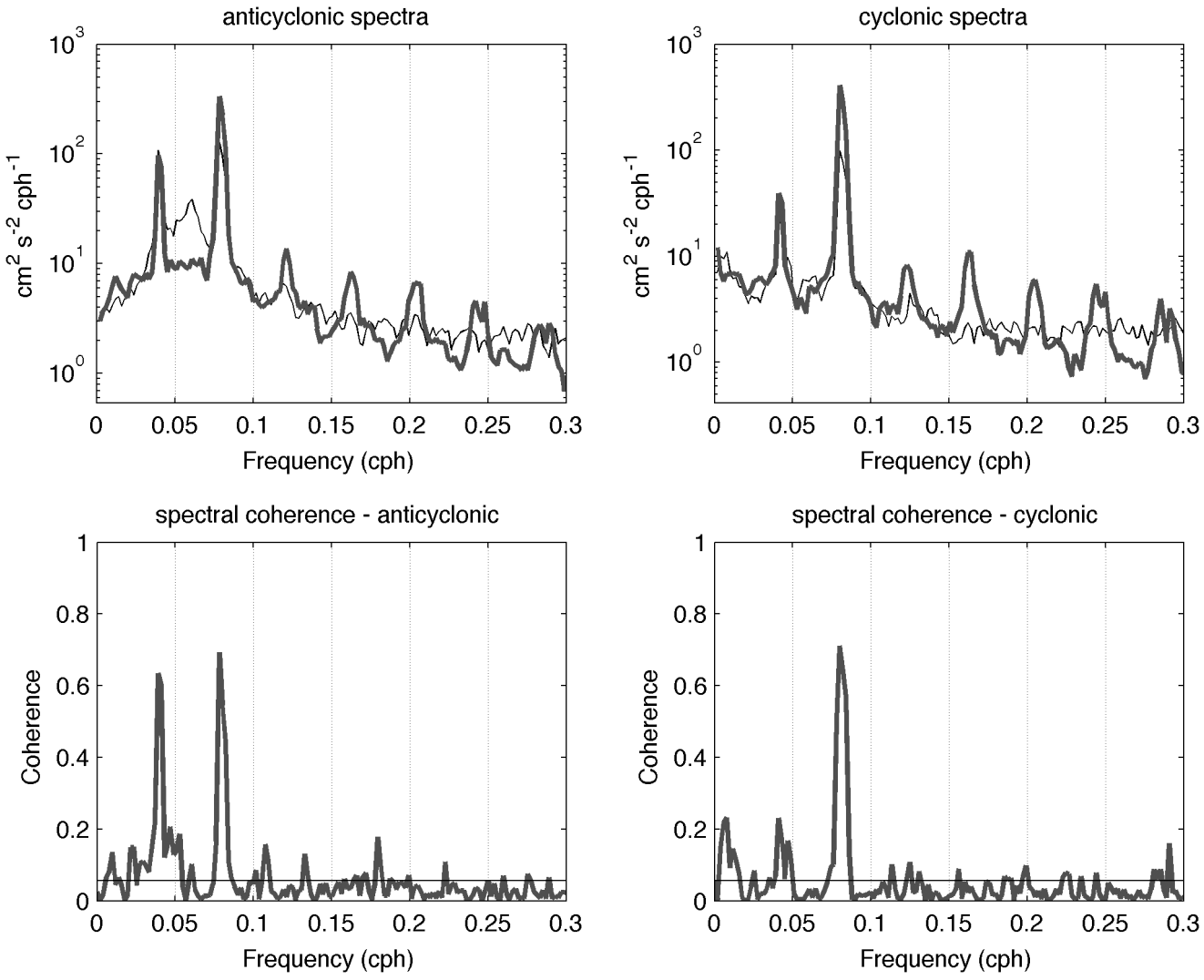

Figure 5. Radar (thin black line) and model (thick gray line) current spectra at the grid point closest to the VIDA buoy location. (top to bottom) anticyclonic (left-hand side) and cyclonic (right-hand side) components of power spectral density for radar (thin black line) and model (thick gray line), and, squared coherence between radar and modeled currents. Horizontal lines in the coherence spectra mark the 95% confidence level.

4.2. Spectral Analyses

[32] Spectral decompositions of radar and model at the grid point closest to the VIDA buoy location, and subsurface ADCP currents for the bin closest to surface and free from interferences with the surface itself, along with their cross-spectral analyses, are presented in Figures 5–7. At this location, model currents (gray thicker line in the uppermost panels) reproduce semidiurnal and diurnal peaks of radar spectra. Although the model (gray line) overestimates the spectral energy density at semidiurnal frequencies (Figure 5), it underestimates the energy in the anticyclonic inertial band at this specific location. This underestimation most likely stems from NAPOM underestimation of density stratification (see "section 5) but could also partly be a consequence of a relatively poor high-frequency reproduction of wind variability by atmospheric forecast model ALADIN/SI. For dominant spectral peaks, coherence values are statistically significant at the 95% confidence level. Model currents also have peaks at frequencies of $\nu \sim 0.125$, 0.16, 0.21, and 0.24 cph (that is, periods of 8 h, 6 h 15 min, 4 h 45 min, and 4 h 10 min). These peaks are more than an order of magnitude smaller than the tidal signal and are most likely model artifacts that are introduced by the wind stress calculation in the model.

[33] Separate comparisons radar-to-ADCP currents, and model-to-ADCP currents are provided in Figure 6 (radar currents, black thin line; ADCP currents, gray thicker line) and Figure 7 (model currents, black thin line; ADCP currents, gray thicker line), respectively. Both comparisons again show good match in dominant semidiurnal and diurnal peaks, and larger discrepancies in the inertial frequency band ($f \sim 0.058$ cph, or $T \sim 17$ h). Radar currents are slightly more energetic in the anticyclonic diurnal and inertial bands, while ADCP currents have slightly more energy in the cyclonic semidiurnal and diurnal bands. Also, ADCP currents tend to have more energy than radar currents at

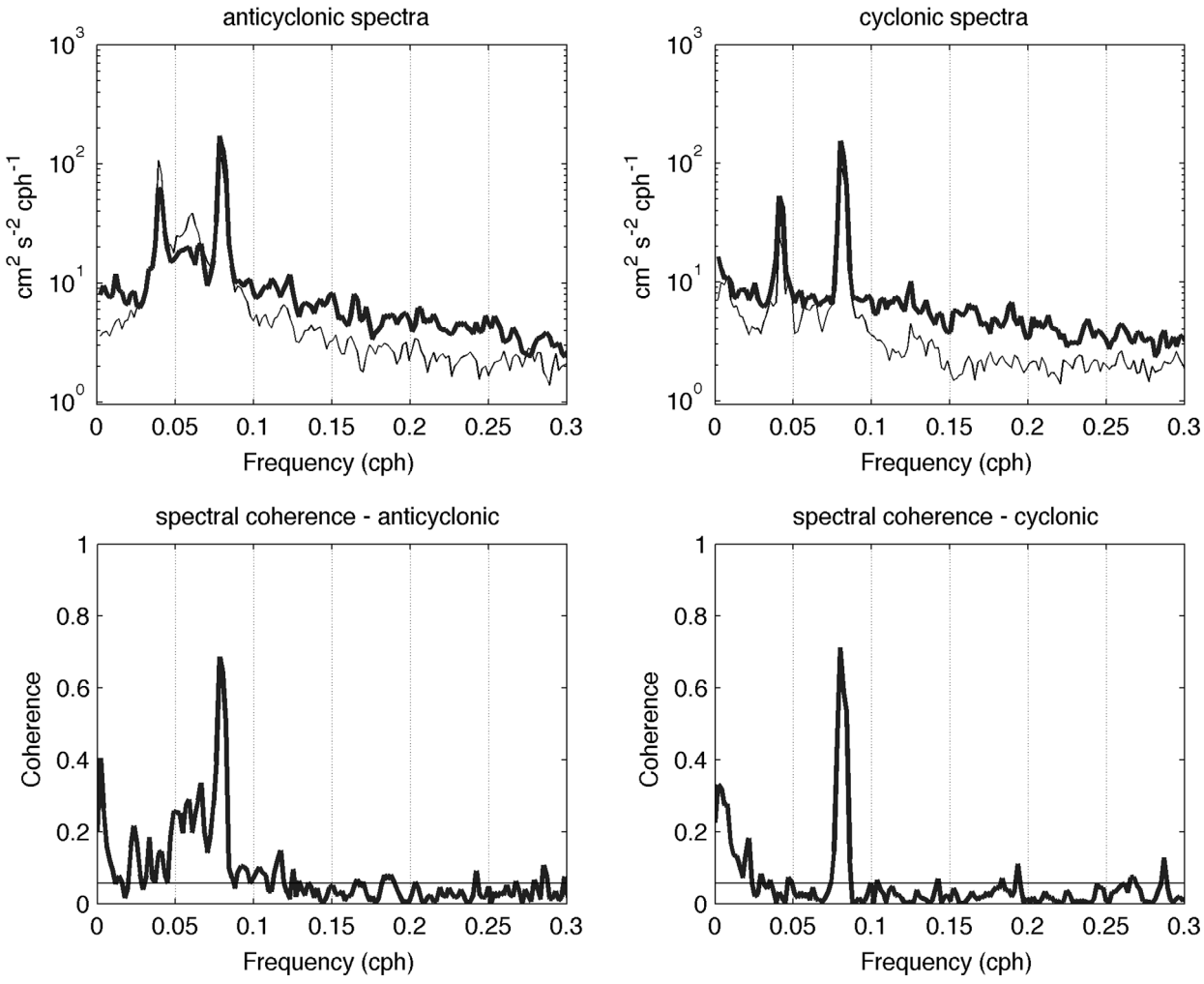

Figure 6. Similar to Figure 5, except that thick gray line represents ADCP currents at 4 m depth.

this location in both the low- and high-frequency tails of the spectra. In comparison with ADCP currents (Figure 7, gray thick line), model currents (thin black line) in the semidiurnal frequency band are slightly more energetic than subsurface velocities in both the cyclonic and anticyclonic spectra, while they have similar amplitudes in the diurnal frequency band for both the cyclonic and anticyclonic spectra. Both radar and model currents in the semidiurnal band show high coherence with ADCP currents in the cyclonic and anticyclonic spectra.

4.3. Tidal Analyses

[34] Of the seven dominant tidal constituents describing the Adriatic Sea tidal variability (M_2, S_2, N_2, K_2, K_1, O_1, and P_1), only the semidiurnal (M_2, and S_2; periods of 12 and 12.42 h, respectively) and the diurnal (K1; period 23.93 h) harmonics have a significant impact on tidal variability in the GoT. Other constituents included in the analysis provided ellipses with major and minor semiaxes at least one order of magnitude smaller than the three above-mentioned constituents. Although different in relative terms (Figure 8), model and radar tidal currents have a similar spatial distribution with a maximum around the SW corner of GoT, and a decreasing influence into the interior of the gulf. In relative terms, tidal variability represents up to 25% total variance for radar currents and more than 30% total variance of modeled currents around the southern part of the entrance to the GoT (Figure 8).

[35] Comparisons with the ADCP data at the VIDA buoy suggest a tendency of modeled currents to overestimate tidal contribution at that specific location (Tables 1 and 2), when compared with currents at Vida (bin 16 above the bottom, equal to the height 17 m above the bottom, or depth around 4 m). At this location, tides represents about 13% of current variability, a value closer to that of radar rather than that of modeled tidal contribution. Phase offsets between radar and modeled currents are negligible ($\Delta\phi = 2°$) for the M_2 constituent, being somewhat larger for the S_2 constituent ($\Delta\phi = 17°$, approximately 34 min temporal offset). Phase differences and corresponding time lags for the buoy-radar pair, are $\Delta\phi = 13°$ for the M_2 constituent (approximately 26 min), and $\Delta\phi = 32°$ for the S_2 constituent (approximately 1 h). For the buoy-model pair, they are $\Delta\phi = 11°$ for the M_2 constituent (approximately 22 min), and $\Delta\phi = 15°$ for the S_2 constituent (approximately 30 min).

[36] The spatial distribution of the M_2 tidal ellipses for radar and model currents (Figure 8) show large variability in amplitude, with elongated ellipses and local maxima in

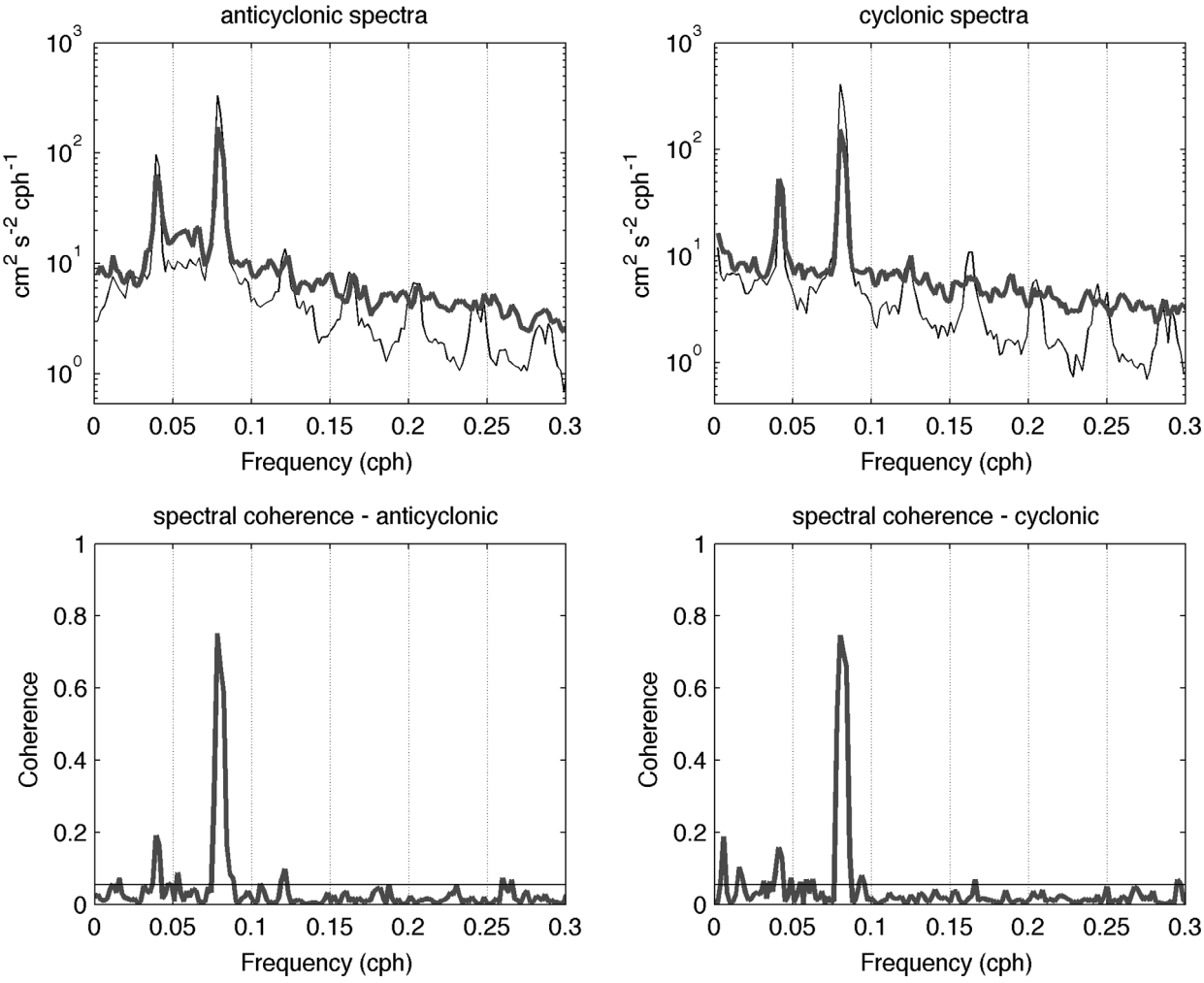

Figure 7. Similar to Figure 5, except that thin lines represent model currents and thick gray lines ADCP currents at 4 m depth.

proximity of the south-eastern corner of the GoT and have a more circular-shaped pattern in the NW part in proximity of the coastal lagoon along the Italian coastline. In the remaining sectors of the GoT, where the radar coverage was good, there is a rather good agreement in major and minor axes of tidal ellipses. The same holds for the sense of rotation of the ellipses and the ellipse inclinations. The S_2 constituent (Figure 8) has very similar spatial distribution to the M_2 constituent in model results as well as in radar measurements.

[37] Discrepancies are found for the diurnal K_1 constituent (Figure 8). Both radar and model K_1 ellipses of current vectors are clockwise rotating in the entire domain. Compared to tidal ellipses from the subsurface current record, both radar and model present significant departure from the ADCP-current ellipses in eccentricity: K_1 ellipse for ADCP currents is significantly more rectilinear than that of radar and model (not shown). Phase offsets and time lags are: $\Delta\phi = -7^\circ$ (27 min lag) for the radar currents with respect to ADCP, and $\Delta\phi = -29^\circ$ (1 h 55 min lag) for the modeled currents against the ADCP data at this location.

4.4. The Empirical Orthogonal Function (EOF) Analysis Decomposition

[38] Out of 524 possible EOF modes, 50 (43) were required to reach the 95% retained variance threshold for radar (model) currents; however, only the first four EOF modes contributed 63% (75%) variance of radar (model) currents (Table 3).

[39] The spatial pattern for the leading EOF-1 for radar (31% variance) and model (46% variance) currents, shown in Figure 9, describes a rather uniform inflow/outflow pattern that matches with time-averaged currents (Figure 2). Some differences are however present, in particular in proximity of the southwestern corner and along the Slovenian coastlines where model amplitudes are lower, and in the GoT interior where the spatial structure of the model EOF-1 presents a more marked cyclonic structure. Modal amplitudes between temporal amplitudes of radar-model EOF-1 show a relatively high correlation ($R = 0.58$). Spectral analyses of the expansion coefficients for this mode show that modal variances are similar for both the radar and model EOF time series (right-most plots in Figure 9) in the semidiurnal and low-frequency band; however, radar

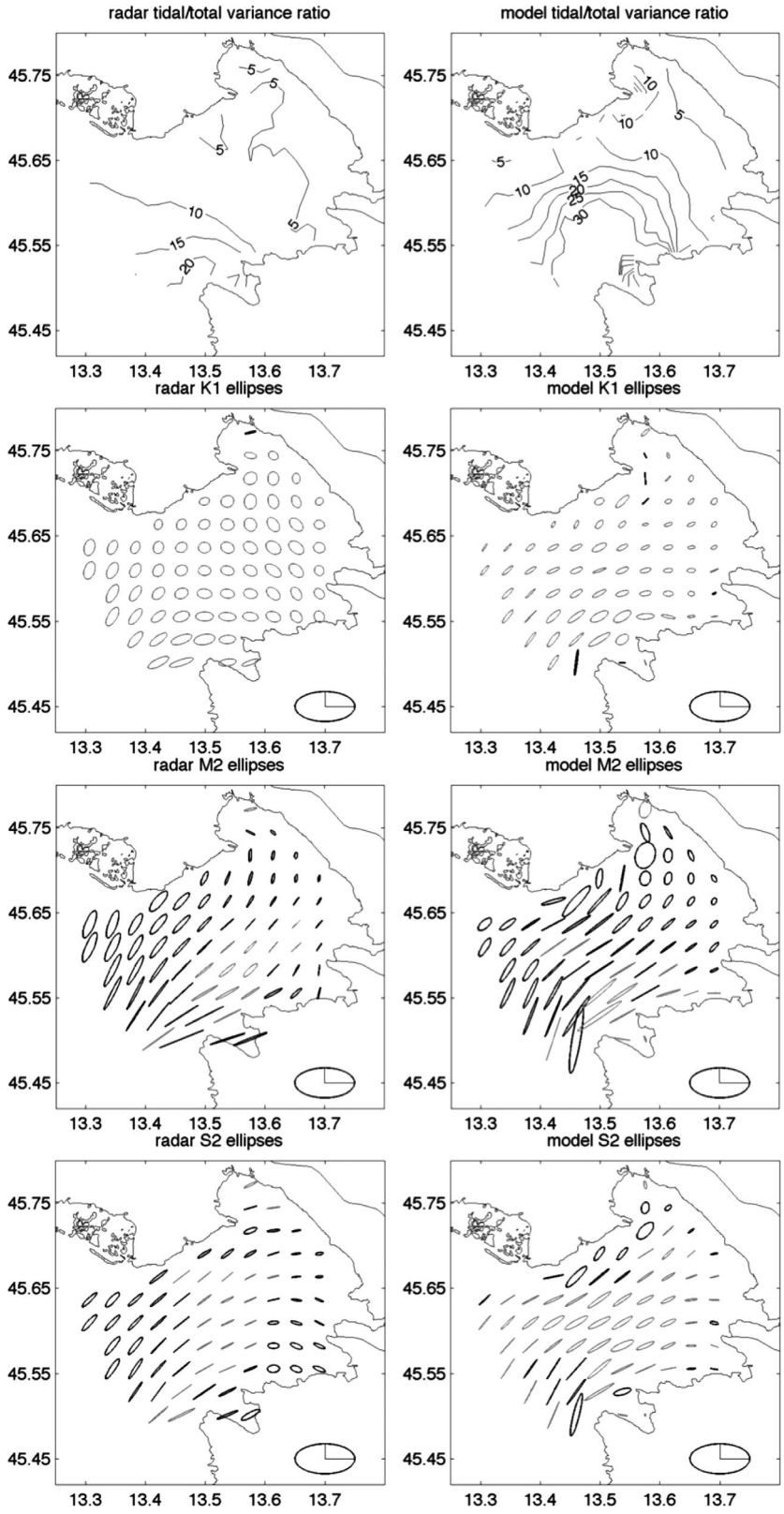

Figure 8. (top to bottom) Spatial distribution of tidally explained variance (percent) of radar and model currents. Spatial patterns of the tidal ellipses for the diurnal (K_1) harmonic. Spatial patterns of the tidal ellipses for the semidiurnal (M_2, S_2) harmonics. Ellipses are plotted in black (gray) if they have counter-clockwise (clockwise) sense of rotation. Amplitude of the scale ellipse is 10 cm/s for the semimajor axis, and 5 cm/s for the semiminor axis. Current ellipses were plotted at every second grid point for clarity.

Table 1. Tidal Analysis Results With Corresponding Confidence Intervals for Radar and Model Currents at the Grid Point Closest to the VIDA Buoy, and ADCP Currents[a]

Constituent	Major Axis	Minor Axis	Inclination	Phase
M_2				
Radar	4.24 ± 0.30	−0.20 ± 0.23	24 ± 4	165 ± 4
Model	7.77 ± 0.23	0.05 ± 0.21	43 ± 1	167 ± 1
Buoy	4.87 ± 0.32	−0.10 ± 0.29	33 ± 3	178 ± 3
S_2				
Radar	2.66 ± 0.29	−0.006 ± 0.26	19 ± 6	151 ± 5
Model	4.58 ± 0.22	0.31 ± 0.25	40 ± 3	168 ± 3
Buoy	3.12 ± 0.24	−0.34 ± 0.23	26 ± 5	183 ± 5
K_1				
Radar	2.51 ± 0.45	−1.38 ± 0.46	356 ± 18	358 ± 17
Model	3.91 ± 0.36	−0.97 ± 0.30	336 ± 5	336 ± 5
Buoy	2.75 ± 0.65	−0.31 ± 0.45	53 ± 10	5 ± 15

[a]Units are cph (cycles per hour) for frequency, cm/s for major, minor axes and errors; degrees for inclination angles and phase errors. The constituent K_1 has a frequency 0.0417807 cph, the M_2 0.0805114 cph, and S_2 0.0833333 cph.

modal coefficients for this EOF mode contain also energy in the inertial frequency band ($f \sim 0.058$ cph). Modal variance spectra suggest thus that the first EOF for both radar and model reconstruct the tidal signal and the lower-frequency variability, with additional components in the inertial band and the diurnal band in the radar data associated with the diurnal sea-breeze wind regime (*Cosoli et al*., 2012b). Inertial peak in the spectra of first four EOF modes of model results is clearly visible, although it is usually about five times lower than that of radar currents, except for the EOF-3, where the match is solid.

[40] EOF-2 explains a similar variance of radar (19.5%) and model (19.7%) currents. Its spatial structure for radar currents shows a rather uniform structure, perpendicular to radar EOF-1 mode, while for model currents EOF-2 it presents a curved, cyclonic pattern, which helps to explain the model time-averaged cyclonic circulation pattern. With respect to radar EOF-2, model spatial pattern presents intensification in the southwestern area along the Slovenian coast. Time series of modal amplitudes have correlation $R = 0.44$, weaker than what is found for EOF-1. Similar to EOF-1 results, they present strong modulations by semidiurnal and diurnal motions, as evidenced in the spectral analysis, with some underestimation within the remaining frequency bands.

[41] EOF mode-3 (6.8% variance for radar currents; 6.6% variance for model currents) show a cyclonic turn in the inner part of the GoT; also, similarly to EOF-2, this mode shows intensification in the SW corner (Piran Bay). One important difference is the following: radar EOF-3 mode shows a stagnation point toward the entrance of the GoT, while the corresponding mode from model does not. Again, as noted for the previous two modes, the temporal variability is modulated by semidiurnal and diurnal components.

Table 2. Total Variance, Tidal Variance, and Ratio Tidal/Total Variance for Surface Radar and Model Currents at the Grid Point Closest to the VIDA Buoy, and Corresponding Variances for ADCP Data[a]

	Total Variance	Tidal Variance	Ratio (%)
Radar	112	16.9	15.1
Model	155	50	32.2
Buoy	156	21	13.4

[a]Units for variances are cm^2/s^2.

[42] While there is a relatively good agreement for the first three EOF modes for both the spatial structures and the associated temporal variability, discrepancies are significantly larger in EOF-4 mode, which in the radar data explains a larger amount of variance than in the model. The vector map for radar spatial pattern (6.6% variance) describes intense anticyclonic circulation occurring at the basin scale of the GoT, while model (3.2% of variance) shows a peculiar sheared flow. Spectral decomposition of modal coefficients shows again the semidiurnal variability for both radar and model; however, radar coefficients for this mode also present contributions from inertial, diurnal, and low-frequency band.

5. Discussion

[43] The paper presents a preliminary analysis of the temporal and spatial distributions of currents in the surface (upper 0.5 m) layer in the Gulf of Trieste.

[44] Radar measurements and model output are both prone to errors. Radar measurements only capture a surface skin layer (approximately 0.5 m thick at the 25 MHz operating frequencies), provide a discontinuous coverage in time and space and are influenced by external interferences and hardware failures, and may inadequately resolve processes at scales finer than the sampling grid. This is especially true for areas such as far range cells where the backscattered echo is relatively low due to signal attenuation with range, with a consequent increase in radar uncertainties, and the radar cross-section increases, resulting in poorly constrained current vectors. However, they provide

Table 3. Summary of the EOF Decomposition of the Radar and Model Currents for the First Four EOF Modes: Percent Variance Retained by Each EOF Mode for Radar and Model Currents, Magnitude of the Correlation Between Temporal Amplitudes of the Radar and Model EOFs of the Same Mode, and Cumulative Variance by Radar and Model EOF Modes

EOF Mode	% Explained Variance—Radar	% Explained Variance—Model	Correlation Magnitude	% Cumulative Variance (radar)	% Cumulative Variance (model)
1	31.0	45.7	0.58	31.0	45.7
2	19.4	19.6	0.44	50.4	65.3
3	6.8	6.6	0.29	57.2	71.8
4	6.6	3.2	0.17	63.8	74.9

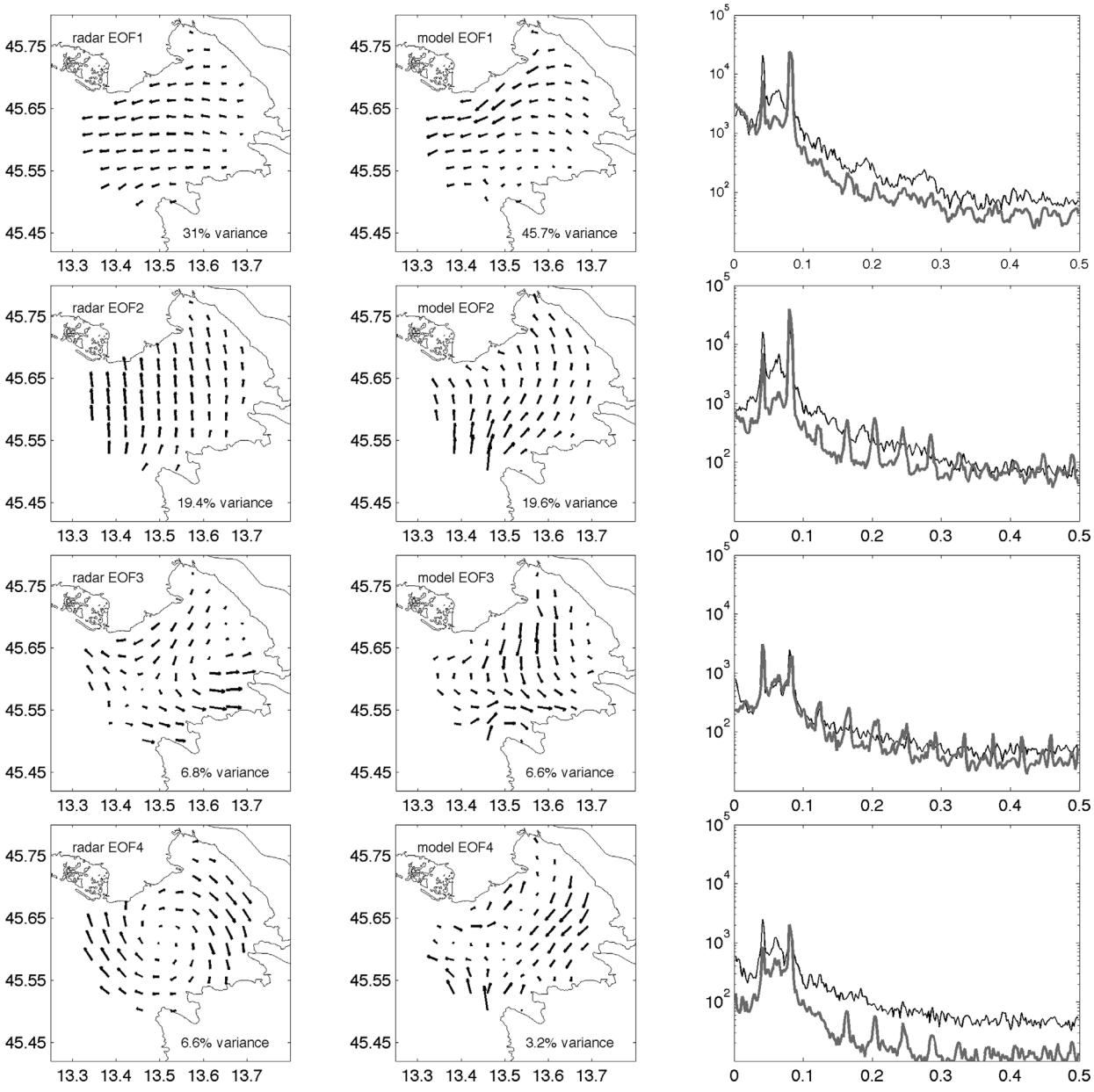

Figure 9. Spatial patterns of the first four dominant EOF modes for (left) radar currents and for (middle) model currents. (right) Spectra of temporal expansion coefficients associated with each mode are also given, thin black lines correspond to the spectral decomposition of radar EOF temporal coefficients, thick gray lines correspond to the spectral decomposition of model EOF temporal coefficients. Units for the frequency axis are cycles per hour (cph). Current vectors were plotted in every second grid point for clarity.

a synoptic view of surface current fields that would not be feasible with more conventional and more accurate but pointwise current meters, or with Lagrangian drifters. Models, on their side, may be affected by the horizontal and vertical grid resolution, inherent drawbacks of their respective grid (e.g., sigma grid), and inaccurate or incomplete parameterization of physical processes in highly variable coastal areas such as the GoT, where the typical current magnitudes are small (0.1 m/s), but are highly variable in time and space due to wind and freshwater input. Regional models are furthermore strongly susceptive to atmospheric forcing and open boundary conditions, both provided by other models burdened with errors.

[45] Nevertheless, the ultimate goal of the proposed work is to show that experimental data from a network of HF radars and numerical simulations from high-resolution numerical models can supplement each other to study the dominant circulation features in the GoT if their intrinsic limitations are taken into account. Numerical models provide often desired spatial and temporal continuity of forecasted ocean currents, while radar observations represent an invaluable tool for obtaining real-time surface current

measurements and provide, in areas with good radar coverage, a solid ground for numerical model skill assessment.

[46] Based on a discontinuous series of vertical current profiles collected in the GoT during the 1979–1981 period, *Stravisi* [1983a, 1983b] proposed a layered gyre-type circulation pattern with a weak (2–3 cm/s) permanent cyclonic (counter clockwise) circulation in the bottom layer (below 10 m depth), and an alternating, wind-driven, cyclonic-anticyclonic flow in the surface (approximately 5 m thick) layer. NAPOM also reproduces to a good extent in its 20 months time-averaged current map the basin-scale cyclonic gyre for the upper layer in the GoT interior, with time-averaged currents of approximately ∼5 cm/s along the Slovenian border and an intensified (10–12 cm/s) coastal jet along the northern Italian coast. The corresponding radar time-averaged current map matches in spatial extension the coastal jet-like structure along the northern border, but with respect to the model it curves more to the NW following the local bathymetry and coastline. No clear evidence of Adriatic water inflow is however found to the south along the Slovenian coast from the monthly averaged current maps. According to the model monthly current maps, the cyclonic circulation, described by previous authors [for instance, *Stravisi*, 1983a, 1983b], is persistent over time (and only weakens in May 2012), with small differences from month to month. However, radar-model discrepancies may be due to the different sampling depth of the radar and the model and the intrinsic interannual variability of mean currents in the surface skin layer as documented by *Bogunović and Malačič*, [2009].

[47] Radar monthly maps also document a complete reversal to a surface anticyclonic gyre in the GoT interior during April and May 2012. An inspection of the temporal evolution of the surface current fields shows that radar and the model both capture this current reversal. Different persistence of the inverted circulation between radar and model is most likely related to the model set-up: monthly climatological river fluxes are used as a freshwater input in the GoT, thus resulting in a gross underestimation of the true riverine contribution with its strong time variability within a month. Even though the climatological discharge for the Isonzo/Soča River (137 m^3/s; source: Slovenian Environment Agency—ARSO) matches the order of magnitude of the time-averaged measured discharge rate (103 m^3/s) for April 2012, the true discharge was not evenly distributed throughout the month and the dynamics of the observed extreme peak discharge of 681 m^3/s was not properly simulated.

[48] One major difference between radar and model time-averaged map is related to current variances. In general, there is a good match in terms of their spatial distributions, with local maxima along the Italian coast to the north where the coastal jet is found, and in proximity of the SE corner at the tip of the Istrian peninsula. Also, model variances show clustering in two main sectors in the GoT as an effect of the shallow local bathymetry and riverine input while, on the other side, radar currents are more evenly distributed in the GoT. In time, both radar and model show a seasonal cycle with maxima during the warm stratified season when the effects of diurnal wind cycle is predominant and when a stable stratification in the water column favors inertial oscillations and somehow enhances also diurnal, as well as semidiurnal current variances (Figure 3). However, variance levels of modeled currents are significantly lower (up to 50% in terms of maximum values) than corresponding values for radar currents for all months except for February 2012. While the radar-model mismatch for this month is attributable to a hardware failure in one of the systems (PIRA) that seriously compromised the observational network performances, a detailed investigation is needed for the remaining period.

[49] Band-pass filtering of model and radar variances shows that the largest differences occur within diurnal and inertial frequency bands, since the model fails to reproduce the magnitude of the observed current variability for these bands. Differences in the low-frequency components are lower for the subtidal, low-frequency band than other selected bands, as is also noticed by the spectral decomposition. Model variances in fact explain 70%, 49%, 44%, and 27% (median percent value) of radar currents in the low-frequency, diurnal, semidiurnal, and inertial frequency bands, respectively. *Cosoli et al*. [2012b] showed from previous HF radar current measurements in the area that a large fraction of the seasonal (spring and summer) variability in the diurnal band is attributable to the seasonal cycle of wind energy in the same frequency band, and that it appears as spectral peak with 24 h periodicity. Similar to the diurnal band energy, *Cosoli et al*. [2012b] described the seasonal and spatial patterns of the inertial-band energy in the NE Adriatic Sea. Inertial oscillations are a common feature in ocean circulation and have been reported and described at many locations in the world's oceans. In the Adriatic Sea, they have been reported offshore in the Venice Lagoon's area [*Kovačević et al*., 2004] and at several offshore locations on the Adriatic shelf during the warm stratified season [*Krajcar and Orlić*, 1995]. A temporal variability in the inertial band has been revealed for the radar data inside the GoT, showing increasing energy content during spring-summer (March–July) and decreasing energy content during fall-winter months (September–February), but it was not reproduced by the model.

[50] A number of explanations can be found for the seasonal modulation in the diurnal and inertial band energy. Contamination by diurnal-band wind energy and leakage into the diurnal tidal constituents (K_1, P_1) and neighboring frequencies explains the observed diurnal-band variability and has also been reported, for instance, in *Rosenfeld* [1988], *Kaplan et al*. [2005], and *Pidgeon and Winant* [2005]. Model-data mismatches in this frequency band have been attributed to model inadequacies in representing a wide spectrum of physical processes (such as meteorological forcing, baroclinic signals, or coastally trapped waves; *Erofeeva et al*. [2003] for the central Oregon shelf; *Rosenfeld et al*. [2009] for the central California area).

[51] For the GoT, the radar-model difference in the horizontal distribution of variance is ascribed to the sigma-layer discretization, the forcing and the inadequate representation of the density stratification in the model. As previously noted, the relatively coarse NAPOM sigma-layer discretization in the surface layer fails in accurately reproducing wind effects. Horizontal gradients of depths cause gradients of the model sigma-layers with modest resolution. Despite this model drawback, there is a correlation in the spatial distribution of current variance since

both model and radar data show local variance maxima in the area of the coastal-jet structure and a decreasing trend of it in south-east direction. Again, this discrepancy is most likely arising from the model's sigma-level discretization. Since NAPOM employs only 11 sigma levels which are not condensed enough near the surface, the surface cells can get as much as 1.2 m thick (the first nonzero sigma-level 0.06 in the 20 m water column). Numerical simulations with a finer vertical layer distribution (not shown here) showed that finer sigma-layer distribution near the surface leads to higher surface current velocities under the same wind forcing. Atmospheric forecast model is also responsible for an imperfect reproduction of hourly winds thus causing a phase mismatch between the observed and modeled inertial signal [see also *Matthews et al*., 2012]. Comparisons between in situ CTD density data (sampled at the VIDA buoy approximately twice per month) and corresponding vertical density profiles from the model revealed that NAPOM is underestimating water column stratification (not shown). In particular, the model fails in reproducing the intense pycnocline during the warm season presenting instead an almost vertically homogeneous water column or a very weak stratification. Calculations of the buoyancy frequencies give differences as high as one order of magnitude between the data and model. Since vertical density stratification confines the inertial band momentum to the surface layer, this model underestimation of stratification during the warm season leads to a systematic underestimation of model surface layer energy in the inertial band.

[52] Although being more pronounced in the radar data than modeled currents, the semidiurnal tidal frequency band shows a seasonal modulation, which is attributed to wind variability in this frequency band. In fact, wind spectra from coastal stations disseminated along the GoT coastline revealed the presence of marked peak in the semidiurnal band, a common feature in surface winds over the globe (50° S–70° N; see for instance *Dai and Deser* [1999]). This hypothesis was also strengthened by a bandpass decomposition similar to that used for radar and model currents, which provided evidences of seasonal modulation in wind data in the semidiurnal frequency band.

[53] High-frequency peaks at frequencies of $\nu \sim 0.125$, 0.16, 0.21, and 0.24 cph (that is, periods of 8 h, 6 h 15 min, 4 h 45 min, and 4 h 10 min) in the model current spectra can be explained in terms of two distinct mechanisms. The first mechanism is related to reflections of barotropic disturbances back into the model domain at the open boundary. Preliminary numerical experiments (not shown here) indicate that this problem might be suitably addressed using the flow relaxation scheme (a high friction buffer zone between NAPOM and its parent model) as the open boundary condition [see e.g., *Engedahl*, 1995]. These high-frequency peaks may also be introduced in the model during conversion from hourly wind speed data to wind stress calculated at each model time step. To support this, spectral analyses were performed on wind records, either from ALADIN data or from coastal stations in the GoT, and then repeated on input wind stress data. Analyses (not given here) showed peaks at semidiurnal, diurnal, and lower frequency bands—but no higher-frequency peaks—were present in both ALADIN and measured winds. Those peaks were, however, present in the wind stresses, computed in NAPOM. Efforts are being made to remove this model drawback which has otherwise very little or no influence on synoptic forecast.

[54] NAPOM includes the Adriatic Sea tidal major constituents, i.e., the four semidiurnal constituents M_2, K_2, N_2, S_2, and the three dominant diurnal constituents K_1, P_1, and O_1, starting from a coarser tidal model of the entire Adriatic and interpolated to the locations of the model open boundary [*Malačič and Viezzoli*, 2000; *Malačič et al*., 2000]. Results of the spectral analyses of both radar and modeled currents evidenced a good agreement for the semidiurnal constituents; however, as mentioned earlier, some larger mismatch is observed in the diurnal frequency band due to contamination by diurnal wind energy.

[55] In general, there is a tendency of the model to overestimate tidal energy in the entire GoT, and in particular in proximity of the SW corner and in proximity of the Isonzo/Soča River. A larger tidal variance of model currents with respect to that of radar currents should not be surprising. NAPOM ocean mixed layer discretization in fact leads to less energetic surface currents, thereby relatively increasing (in comparison to the radar currents) the tidal influence on the total variance of the model currents.

[56] As confirmed by the least-squares tidal analyses, the semidiurnal peaks are centered on M_2 and S_2, the contributions of the other semidiurnal constituents being typically one order of magnitude smaller and are thus negligible. For the semidiurnal frequencies, model and radar currents show a similar partition between cyclonic and anticyclonic energy, resulting in highly eccentric current ellipses in the majority of the GoT. This is in agreement with previous numerical simulation studies and observations. Solid match between ellipse orientation, major and minor axis amplitudes, and phases are also observed. The same holds for a match with *Malačič and Viezzoli* [2000] for the sense of rotation, although the radar current better matches the previously proposed rotation pattern. Differences are observed in proximity of the Isonzo/Soča river outlet, where model ellipses show larger amplitudes and more circular shapes than the radar ellipses, and in the NW corner of the domain, where radar ellipse orientations more closely follows the coastline orientation. Diurnal peaks are centered on the K_1 and, particularly for radar currents, on frequency of exactly 1 cycle/day (cpd), which severely biases any comparison between the model and the data as already mentioned above. Thus, any direct comparison between radar and model cannot be considered "unbiased". However, despite "contamination", both radar and model show prevalence of clockwise energy, resulting in circular and clockwise-rotating ellipses. While radar data show a marked circular pattern, model K_1 ellipses present a more rectilinear pattern offshore Piran matching thus more closely results from previous studies [*Malačič and Viezzoli*, 2000; *Cushman-Roisin and Naimie*, 2002].

6. Conclusions

[57] Surface currents from HF radar measurements in the Gulf of Trieste (GoT) in the northeastern Adriatic, were compared to high-resolution model simulations. The model used realistic meteorological forcing and included tidal oscillations and climatological data for freshwater input in the GoT. Despite some limitations, results show that the

model was successful in capturing dominant circulation features and the observed dynamics in the GoT, although underestimating the overall observed variances. The model underestimated the temporal variability in the inertial and diurnal frequency band due to underestimated representation of vertical stratification in the warm season. In the semidiurnal frequency band, good agreement was observed between model and radar data. The comparison was poorer for the K_1 diurnal constituent, most likely due to contamination in the surface radar currents from diurnal signals at neighboring frequencies and diurnal-band wind energy. Discrepancies were also observed between the sampled data and the model simulations during April and May 2012, when a sub-basin anticyclonic gyre was observed in radar measurements in coincidence with an increased freshwater input in the GoT. Inadequacies in the model capabilities to fully reproduce this peculiar current pattern can be attributed to the climatological freshwater input. We aim to reduce these model insufficiencies by additional coupling of NAPOM to a standalone hydrological discharge model of the Isonzo/Soča River, which is underway. Also, the relatively coarse sigma layer vertical resolution under the present model configuration is deemed responsible for a reduced energy content in modeled surface currents.

[58] In summary, this study constitutes an encouraging step toward a combined use of remotely sensed surface currents to the validation and calibration of high-resolution coastal ocean models. Numerical models supplement radar observations in poor radar coverage areas and ensure 3-D spatial and temporal continuity of currents and water masses distribution forecasts (and analyses). High-frequency radars are however invaluable in revealing numerical model drawbacks in areas with good radar coverage and areas with stronger topographic gradients.

[59] **Acknowledgments.** Flow rates for the Isonzo/Soca River were derived from the hydrometric level data measured by the station positioned 14 km upstream of the river mouth. Data were kindly provided by the Direzione Regionale dell'Ambiente (Unita' Operativa Idrografica di Udine) of Regione Friuli Venezia Giulia that also provided wind records in the GoT and surrounding coastal stations. Climatological discharges of the Isonzo/Soca River were provided by Slovenian Environment Agency—ARSO. We are also grateful to the Community of Piran, the Trieste harbor's pilot station, and the "Saturnia Rowing Club" for allowing the radar installation during the project. The manuscript benefitted from discussions with two anonymous reviewers. This work was partially funded under the sponsorship Italia-Malta Programme–Cohesion Policy 2007-2013.

References

Artegiani, A., D. Bregant, E. Paschini, N. Pinardi, F. Raicich, and A. Russo (1997), The Adriatic Sea general circulation. Part II: Baroclinic circulation structure, *J. Phys. Oceanogr.*, *27*, 1515–1532.

Barrick, D. E., and B. J. Lipa (1997), Evolution of bearing determination in HF current mapping radars, *Oceanography*, *10*, 72–75.

Bogunović, B., and V. Malačič (2009), Circulation in the Gulf of Trieste: Measurements and model results, *Il Nuovo Cimento*, *31*, 301–326, doi: 10.1393/ncc/i2008-10310-9.

Boldrin, A., S. Carniel, M. Giani, M. Marini, F. Bernardi Aubry, A. Campanelli, F. Grilli, and A. Russo (2009), Effects of bora wind on physical and biogeochemical properties of stratified waters in the northern Adriatic, *J. Geophys. Res.*, *114*, C08S92, doi:10.1029/2008JC004837.

Book, J. W., R. P. Signell, and H. Perkins (2007), Measurements of storm and nonstorm circulation in the northern Adriatic: October 2002 through April 2003, *J. Geophys. Res.*, *112*, C11S92, doi:10.1029/2006JC003556.

Book, J. W., H. Perkins, and M. Wimbush (2009), North Adriatic tides: Observations, variational data assimilation modeling, and linear tide dynamics, *Geofizika*, *26*(2), 115–143.

Chapman R. D., and H. C. Graber (1997), Validation of HF radar measurements, *Oceanography*, *10*(2), 76–79.

Chavanne, C., I. Janeković, P. Flament, P.-M. Poulain, M. Kuzmić, and K.-W. Gurgel (2007), Tidal currents in the northwestern Adriatic: High-frequency radio observations and numerical model predictions, *J. Geophys. Res.*, *112*, C03S21, doi:10.1029/2006JC003523.

Cosoli, S., M. Gačić, and A. Mazzoldi (2005), Comparison between HF radar current data and moored ADCP currentmeter, *Nuovo Cimento*, *28C*(6), 865–879, doi:10.1393/noc/i200510032-6.

Cosoli, S., A. Mazzoldi, and M. Gačić (2010), Validation of surface current measurements in the northern Adriatic Sea from high frequency radars, *J. Atmos. Oceanic Technol.*, *27*, 908–919, doi:10.1175/2009JTECHO680.1.

Cosoli, S., G. Bolzon, and A. Mazzoldi (2012a), A real-time and offline quality control methodology for SeaSonde high-frequency radar currents, *J. Atmos. Oceanic Technol.*, *29*(9), 1313–1328, doi:10.1175/JTECH-D-11-00217.1.

Cosoli, S., M. Gačić, and A. Mazzoldi (2012b), Surface current variability and wind influence in the northeastern Adriatic Sea as observed from high-frequency (HF) radar measurements, *Cont. Shelf Res.*, *33*, 1–13.

Covelli, S., R. Piani, J. Faganeli, and A. Brambati (2004), Circulation and suspended matter distribution in a microtidal deltaic system: The Isonzo river mouth (northern Adriatic Sea), *J. Coastal Res.*, *20*, 130–140.

Cushman-Roisin B., and C. E. Naimie (2002), A 3D finite-element model of the Adriatic tides, *J. Mar. Sys.*, *37*, 279–297.

Cushman-Roisin, B., K. A. Korotenko, C. E. Galos, and D. E. Dietrich (2007), Simulation and characterization of the Adriatic Sea mesoscale variability, *J. Geophys. Res.*, *112*, C03S14, doi:10.1029/2006JC003515.

Dai, A., and C. Deser (1999), Diurnal and semidiurnal variations in global surface wind and divergence fields, *J. Geophys. Res.*, *104*(D24), 31,109–31,125, doi:10.1029/199JD900927.

Davies, A. M., P. Hall, M. J. Howarth, P. J. Knight, and R. J. Player (2000), Comparison of observed (HF Radar and ADCP Measurements) and computed tides in the north channel of the Irish Sea, *J. Phys. Oceanogr.*, *31*, 1764–1785.

Defant, A. (1914), Zur theorie der gezeiten im adriatischen meere, *Ann. Hydrogr. Mar. Meteorol.*, *42*, 270–281.

de Paolo, T., and E. Terrill (2007), Skill assessment of resolving ocean surface current structure using compact-antenna-style HF radar and the MUSIC direction-finding algorithm, *J. Atmos. Oceanic Technol.*, *24*, 1277–1300.

Dorman, C. E., et al. (2006), February 2003 marine atmospheric conditions and the bora over the northern Adriatic, *J. Geophys. Res.*, *111*, C03S03, doi:10.1029/2005JC003134.

Emery, W. J., and R. E. Thomson (2001), *Data Analysis Methods in Physical Oceanography*, 2nd and revised ed., Elsevier, Amsterdam.

Emery, B. M., L. Washburn, J. A. Harlan (2004), Evaluating radial current measurements from CODAR high-frequency radars with moored current meters, *J. Atmos. Oceanic Technol.*, *21*(8), 1259–1271.

Engedahl, H. (1995), Use of the flow relaxation scheme in a three dimensional baroclinic ocean model with realistic topography, *Tellus*, *47A*, 365–382, ISSN: 0280 6495.

Erofeeva, S. Y., G. D. Egbert, and P. M. Kosro (2003), Tidal currents on the central Oregon shelf: Models, data, and assimilation, *J. Geophys. Res.*, *108*(C5), 3148, doi:10.1029/2002JC001615.

Gačić, M., V. Kovačević, S. Cosoli, A. Mazzoldi, J. D. Paduan, I. Mancero Mosquera, and S. Yari (2009), Surface current patterns in front of the Venice Lagoon, *Estuarine Coastal Shelf Sci.*, *82*, 485–494, doi:10.1016/j.ecss.2009.02.012.

Gurgel, K. W. (1994), Shipborne measurements of surface current fields by HF radars, *L'onde Electrique*, *74*, 54–59.

Hopkins, T. S., A. Artegiani, C. Kinder, and R. Pariante (1999), A discussion of the Northern Adriatic circulation and flushing times as determined from the ELNA hydrography, in *Ecosyst. Res. Rep. 32—the Adriatic Sea*, Proceedings of the workshop 'Physical and biogeochemical processes in the Adriatic Sea, Portonovo, 23–27 April 1996, Italy, edited by T. S. Hopkins et al., pp. 85–106, Off. for Off. Publ. of the Eur. Commun., Luxembourg.

Janeković, I., and M. Kuzmić (2005), Numerical simulation of the Adriatic Sea principal tidal constituents, *Ann. Geophys.*, *23*, 1–12.

Kaihatu, J. M., R. A. Handler, G. O. Marmorino, L. K. Shay (1998), Empirical orthogonal function analysis of ocean surface currents using

complex and real-vector methods, *J. Atmos. Oceanic Technol.*, *15*, 927–941.

Kaplan, D. M., J. Largier, and L. W. Botsford (2005), HF radar observations of surface circulation off Bodega Bay (northern California, USA), *J. Geophys. Res.*, *110*, C10020, doi:10.1029/2005JC002959.

Kohut, J. T., and S. M. Glenn (2003) Improving HF surface current measurements with measured antenna beam patterns, *J. Atmos. Oceanic Technol.*, *20*, 1303–1316.

Kovačević, V., M. Gačić, A. Mazzoldi, G. Dallaporta, and A. Gaspari (2000), Sea surface currents measured by coastal HF radar offshore Ancona, *Boll. Geofis. Teor. Appl.*, *41*, 339–355.

Kovačević, V., M. Gačić, I. Mancero Mosquera, A. Mazzoldi, and S. Marinetti (2004), HF radar observations in the northern Adriatic: Surface current field in front of the Venetian Lagoon, *J. Mar. Syst.*, *51*, 95–122, doi:10.1016/j.jmarsys.2004.05.026.

Krajcar, V., and M. Orlić (1995), Seasonal variability of inertial oscillations in the Northern Adriatic, *Cont. Shelf Res.*, *15*, 1221–1233.

Kundu, P. K. (1976), Ekman veering observed near the ocean bottom, *J. Phys. Oceanogr.*, *6*, 238–242.

Laws, K., D. M. Fernandez, and J. D. Paduan (2000), Simulation-based evaluations of HF radar ocean current algorithms, *IEEE J. Oceanic Eng.*, *25*, 481–491.

Malačič, V., and D. Viezzoli (2000), Tides in the northern Adriatic Sea—The Gulf of Trieste, *Nuovo Cimento Soc. Ital. Fis. C*, *23*(C4), 365–382.

Malačič, V., and B. Petelin (2009), Climatic circulation in the Gulf of Trieste (northern Adriatic), *J. Geophys. Res.*, *114*, C07002, doi:10.1029/2008JC004904.

Malačič, V., M. Ceklio, and J. J. Naudin (1999), Dynamics of the surface water in the Gulf of Trieste (Northern Adriatic) during drifting experiments, in *Ecosyst. Res. Rep. 32—the Adriatic Sea, Proceedings of the workshop 'Physical and biogeochemical processes in the Adriatic Sea', Portonovo, 23–27 April 1996, Italy*, edited by T. S. Hopkins et al., pp. 117–125, Off. for Off. Publ. of the Eur. Commun., Luxembourg.

Malačič, V., D. Viezzoli, and B. Cushman-Roisin (2000), Tidal dynamics in the northern Adriatic Sea, *J. Geophys. Res.*, *105*(C11), 26,265–26,280.

Malačič, V., M. Celio, B. Cermelj, A. Bussani, and C. Comici (2006), Interannual evolution of seasonal thermohaline properties in the Gulf of Trieste (northern Adriatic) 1991–2003, *J. Geophys. Res.*, *111*, C08009, doi:10.1029/2005JC003267.

Malačič, V., B. Petelin, and M. Vodopivec (2012), Topographic control of wind-driven circulation in the northern Adriatic, *J. Geophys. Res.*, *117*, C06032, doi:10.1029/2012JC008063.

Matthews, D., B. S. Powell, and I. Janeković (2012), Analysis of four-dimensional variational state estimation of the Hawaiian waters, *J. Geophys. Res.*, *117*, C3, doi:10.1029/2011JC007575.

Mau, J.-C., D.-P. Wang, D. S. Ullman, and D. L. Codiga (2007), Comparison of observed (HF radar, ADCP) and model barotropic tidal currents in the New York Bight and Block Island Sound, *Estuarine Coastal Shelf Sci.*, *72*, 129–137.

Mihanović, H., S. Cosoli, I. Vilibić, D. Ivanković, V. Dadić, and M. Gačić (2011), Surface current patterns in the northern Adriatic extracted from high-frequency radar data using self-organizing map analysis, *J. Geophys. Res.*, *116*, C08033, doi:10.1029/2011JC007104.

Paduan, J. D., and H. C. Graber (1997), Introduction to high-frequency radar: Reality and myth, *Oceanography*, *10*, 36–39.

Pawlovitz, R., B. Beardsley, and S. Lentz (2002), Classical tidal harmonic analysis including error estimates in MATLAB using T_TIDE, *Comput. Geosci.*, *28*, 929–937.

Pidgeon, E. J., and C. D. Winant (2005), Diurnal variability in currents and temperature on the continental shelf between central and southern California, *J. Geophys. Res.*, *110*, C03024, doi:10.1029/2004JC002321.

Pristov, N., J. Cedilnik, B. Strajnar, J. Jerman, M. Štrajhar, and B. Muri (2011), ALADIN related activities in SLOVENIA-2011, paper presented at 21st ALADIN Workshop and HIRLAM All Staff Meeting, Swed. Meteorol. and Hydrol. Inst., Norrkoping, Sweden, 5–8 April.

Querin, S., A. Crise, D. Deponte, and C. Solidoro (2006), Numerical study of the role of wind forcing and freshwater buoyancy input on the circulation in a shallow embayment (Gulf of Trieste, Northern Adriatic Sea), *J. Geophys. Res.*, *111*, C03S16, doi:10.1029/2006JC003611.

Raicich, F., V. Malačič, M. Celio, D. Giaiotti, C. Cantoni, R. R. Colucci, B. Čermelj, and A. Pucillo (2013), Extreme air-sea interactions in the Gulf of Trieste (Northern Adriatic) during the strong bora event in winter 2012, *J. Geophys. Res.*, *118*, doi:10.1002/jgrc.20398.

Rosenfeld, L. K. (1988), Diurnal period wind stress and current fluctuations over the continental shelf off northern California, *J. Geophys. Res.*, *93*(C3), 2257–2276, doi:10.1029/JC093iC03p02257.

Rosenfeld, L., I. Shulman, M. Cook, J. D. Paduan, and L. Shulman (2009), Methodology for a regional tidal model evaluation, with application to central California, *Deep Sea Res., Part II*, *56*, 199–218.

Simpson, J. H. (1997), Physical processes in the ROFI regime, *J. Mar. Syst.*, *12*, 3–15.

Stewart, R. H., and J. W. Joy (1974), HF radio measurement of surface currents, *Deep Sea Res. Oceanogr. Abstr.*, *21*, 1039–1049.

Stravisi, F. (1983a), Some characteristics of the circulation in the Gulf of Trieste, *Thalassia Jugosl.*, *19*(1–4), 355–363.

Stravisi, F. (1983b), The vertical structure annual cycle of the mass field parameters in the Gulf of Trieste, *Boll. Oceanogr. Teor. Appl., I*, *3*, 239–250.

Wang, X., Y. Chao, C. Dong, J. Farrara, Z. Li, J. C. McWilliams, J. D. Paduan, and L. K. Rosenfeld (2009), Modeling tides in Monterey Bay, California, *Deep Sea Res., II*, *56*, 219–231.